

The Formation of Planets by Gravitational Instability in Protoplanetary Discs

Adam Fenton

March 2021

Abstract

Exoplanet survey missions have identified a collection of high mass planets at large orbital radii in excess of 100 AU. These ‘cold Jupiters’, with masses in excess of $1 M_J$, challenge the core accretion model of planet formation. At large distance from their host star, planets would need a few Myr to form by core accretion, potentially longer than the lifetime of the disc. We aim to investigate the formation of these planets by disc fragmentation which occurs within the first few kyrs of evolution. We initially investigate the effect of the numerical viscosity employed in SPH simulations of discs. We simulate discs with varying artificial viscosity (0.1, 0.5, and 1) and we estimate the actual effective viscosity that they introduce in the disc. We calculate effective viscosity by applying an analytical model of disc evolution and comparing the resulting values of effective viscosity to those calculated using the SPH formalism. We find that the value of the effective viscosity in SPH simulation of discs is uncertain, as different methods provide results that differ by approximately an order of magnitude. The values calculated by the analytical model also do not show the expected variance between simulations with different values of artificial viscosity. This could be attributed to a numerical viscosity present in discs with low α_{SPH} which could result in a larger value of “background” effective viscosity

Contents

1	Background and Context	4
2	Project Aims	7
3	Numerical Hydrodynamics	8
3.1	Smoothed Particle Hydrodynamics (SPH)	8
3.2	Meshless Hydrodynamics	10
4	Viscosity treatments in hydrodynamic simulations	12
4.1	Standard artificial viscosity in SPH	12
4.2	Morris and Monaghan formulation	13
4.3	The Balsara switch	13
4.4	The Cullen and Dehnen 2010 (CD10) switch	14
4.5	Viscosity treatment with the Reimann approach	15
5	Protostellar Disc Initial Conditions	16
5.1	Surface and Volume Density	16
5.2	Disc Temperature	18
5.3	Disc Rotation	19
6	Evaluating the effective disc viscosity in SPH simulations	21
7	Future work	28
8	Timeplan	29
9	Thesis Structure	30

1 Background and Context

The number of known exoplanets has increased significantly in the last decade, largely owing to the Kepler space telescope (2009 - 2018) that contributed around 60% of the known planets to the current catalogue. The Transiting Exoplanet Survey Satellite (TESS) launched in 2018 to continue the search for exoplanets in an all sky survey over its two year primary mission. A small fraction of observed exoplanets are confirmed to have masses greater than $1 M_J$ and orbital radii in excess of 100 AU. These planets largely discovered by direct imaging, not by the transit method used by both Kepler and TESS. For a planet to be confirmed by the transit method two transits of the host star are required, the time between them gives the orbital period of the planet. For planets at radii greater than 100 AU, the orbital period is approximately 1000 years and therefore the transit method is an unrealistic mode of detection. Direct imaging allows for the detection of planets on wide orbits without the requirement to observe them for several transits.

The formation of massive planets on such wide orbits is a question that the core accretion (CA) model of planet formation struggles to answer. The CA model describes the gradual accumulation of dust and gas, forming larger and larger bodies until a rocky core has sufficient gravity to accrete a gaseous envelope. For large planets, this mechanism may take several Myrs, a timescale that may exceed the lifetime of the disc.

The fraction of optically thick discs around stars in clusters has been estimated using observations from both ground-based and space-borne telescopes. An ensemble of this data is presented in Fig. 1. An approximate disc lifetime can be determined from this data by observing the fall in disc fraction. Though there are large uncertainties associated with the disc fractions, they reach 50% after 3 Myrs and there is a significant fall-off after 6 Myrs which implies a disc lifetime of 3-5 Myrs (Armitage 2010).

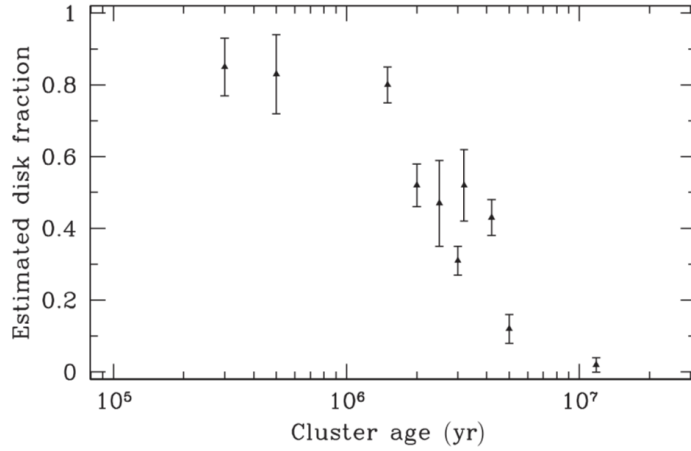


Figure 1: Ground based IR and Spitzer photometry of young clusters, NGC 2024, Trapezium Cluster, NGC 2264, NGC 2362 (Haisch, Jr., Lada & Lada 2001), NGC 1333 (Gutermuth et al. 2008), σ -ori (Hernandez et al. 2007), IC 348 (Lada et al. 2006), Tr 37, NGC 7160 (Sicilia-Aguilar et al. 2006) and Chamaeleon (Damjanov et al. 2007). Figure from Armitage (2010).

Fig. 2 shows the masses of the observed exoplanets plotted as a function of their orbital radius. The so called ‘cold Jupiters’ are marked in red. These objects are those in the dataset that have masses in excess of $1 M_J$ and orbit at radii greater than 100 AU. The surface density of the disc decreases with radius, meaning there is less material at these radii available to form planets. As a result, forming cold Jupiters by CA may be incompatible with estimated disc lifetimes. Planet formation via disc instability has the potential to form planets on timescales of a few kyrs. This avenue of planet formation offers a potential explanation for giant planets forming on wide orbits, in excess of 100 AU.

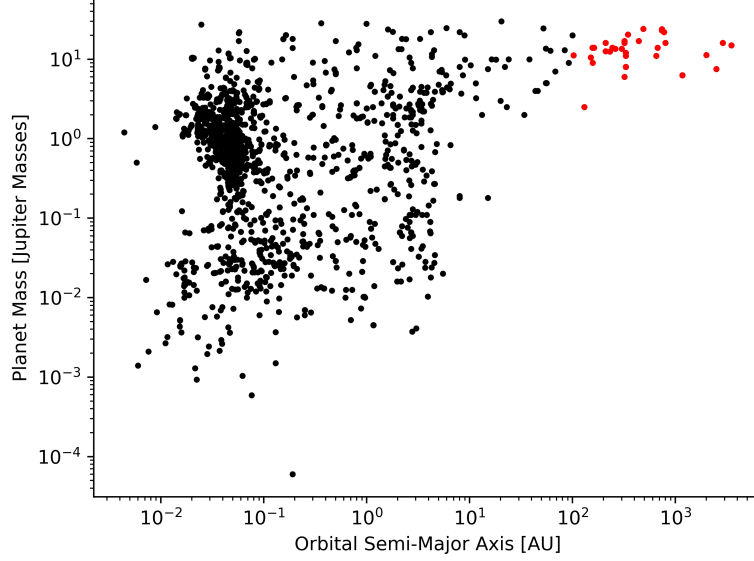


Figure 2: All currently known exoplanets masses plotted as a function of the orbital radius of the planet. The ‘cold Jupiters’ are those that have masses greater than 1 M_J and orbit at radii greater than 100 AU. Plotted with data provided by NASA (2021).

For disc instabilities to develop and fragmentation to occur, the disc must satisfy the Toomre condition such that $Q < Q_{crit}$ where Q is the Toomre parameter,

$$Q = \frac{c_s \Omega}{\pi G \Sigma}, \quad (1)$$

where c_s is the sound speed, Ω is the angular velocity and Σ is the surface density. Q_{crit} is generally accepted to be equal to 1 for axisymmetric discs (Dodson-Robinson et al. 2009; Boss 2011). Additionally, the disc must cool on a sufficiently short timescale; if the cooling time is too long, clumps fail to form. The cooling time is required to be lower or similar to the local dynamical timescale.

2 Project Aims

The aim of this project is to investigate giant planet formation via disc instability, implementing the radiative transfer model of Stamatellos & Whitworth (2009), using the hydrodynamics code PHANTOM. We will improve upon the current treatment of planet formation using polytropic models to track self-gravitating clumps as they evolve within the disc. As these clumps evolve to planets, interactions within different regions of the disc will result in changes to their properties. We will investigate how these properties compare with those of observed exoplanets. A major section of the initial work of this project is concentrated on determining the effective viscosity, α_{ss} , in discs. We compare the values of α_{ss} calculated using an analytical model of disc evolution to those calculated by the SPH formalism presented in Price et al. (2018).

3 Numerical Hydrodynamics

Hydrodynamic simulations are used to investigate the evolution of protoplanetary discs using theoretical models. The results from simulations can then be compared to observations. Such simulations have been carried out using Lagrangian Smoothed Particle Hydrodynamics (SPH) codes such as GANDALF (Hubber, Rosotti & Booth 2018), GADGET (Springel 2005), and PHANTOM (Price et al. 2018), or Eulerian, grid based methods such as ATHENA (Stone et al. 2008). There have also been recent developments in using moving-mesh methods in context of astrophysical problems, an example of which is the code AREPO (Weinberger, Springel & Pakmor 2019). GIZMO (Hopkins 2015) introduces two new meshless methods that aim to improve upon the failings of previous approaches. GIZMO operates in 3 different modes, smoothed particle hydrodynamics and two new meshless methods, meshless finite mass and meshless finite volume, hereafter SPH, MFM and MFV, respectively. SPH has seen use in a wide range of problems including simulations of protoplanetary discs (Mercer & Stamatellos 2020; Cadman et al. 2020). This section will focus on each of these methods in turn, highlighting both their merits and their drawbacks.

3.1 Smoothed Particle Hydrodynamics (SPH)

SPH is a Lagrangian method meaning that the set of elements that discretize the fluid move with the flow. The elements are represented as particles which are Dirac δ - functions smoothed over some smoothing length h using a smoothing kernel W which must satisfy

$$\int_V W(\mathbf{r} - \mathbf{r}', h) d\mathbf{r}' = 1, \quad (2)$$

where both \mathbf{r} and \mathbf{r}' range over a volume V . This kernel function is such that in the limit of h approaching zero, it reduces to the Dirac δ - function (Lodato & Cossins 2011),

$$\lim_{h \rightarrow 0} W(\mathbf{r} - \mathbf{r}', h) d\mathbf{r}' = \delta(\mathbf{r} - \mathbf{r}'), \quad (3)$$

where h is calculated with the assertion that a sphere of radius $2h$ centred around an SPH particle must contain a specific number of neighbours, N_{neigh} . In SPH, any quantity $A(\mathbf{r})$ can be expressed as a function of the values it takes at each of the particle locations so that

$$A(\mathbf{r}) = \int_V A(\mathbf{r}') W(\mathbf{r} - \mathbf{r}', h) d\mathbf{r}', \quad (4)$$

Using the density $\rho(\mathbf{r})$, Eq. (4) is equivalent to

$$A(\mathbf{r}) = \int_V \frac{A(\mathbf{r}')}{\rho(\mathbf{r}')} W(\mathbf{r} - \mathbf{r}', h) \rho(\mathbf{r}') d\mathbf{r}'. \quad (5)$$

To discretize a continuous fluid with particles of total mass $m = \rho(\mathbf{r}')d\mathbf{r}'$, we make the SPH approximation by taking the sum over all particles so that Eq. (5) becomes

$$A(\mathbf{r}_a) = \sum_b \frac{m_b}{\rho_b} A(\mathbf{r}_b) W_{ab}, \quad (6)$$

where $A(\mathbf{r})$ is the value of any function A at position \mathbf{r}_a , m_a is the mass of the particle a at position \mathbf{r}_a with density ρ_a and where W_{ab} is equal to $W(\mathbf{r}_a - \mathbf{r}_b, h)$. The SPH form of the continuity equation is trivially found using Eq. (6) such that the density at particle a is

$$\begin{aligned} \rho_a &= \sum_b \frac{m_b}{\rho_b} \rho_b W(\mathbf{r}_a - \mathbf{r}_b, h) \\ &= \sum_b m_b W(\mathbf{r}_a - \mathbf{r}_b, h) \\ &= \sum_b m_b W_{ab} \end{aligned} \quad (7)$$

The equation of motion in its SPH form be derived using Eq. (6)

$$\frac{dv_a}{dt} = - \sum_b m_b \left(\frac{P_b}{\rho_b^2} + \frac{P_a}{\rho_a^2} + \Pi_{ab} \right) \nabla_a W_{ab}, \quad (8)$$

Finally, the rate of change of thermal energy per unit mass in SPH form for particle a is given by

$$\frac{du_a}{dt} = \frac{1}{2} \sum_b m_b \left(\frac{P_b}{\rho_b^2} + \frac{P_a}{\rho_a^2} + \Pi_{ab} \right) \mathbf{v}_{ab} \cdot \nabla_a W_{ab}, \quad (9)$$

where P is pressure, ρ is density, m is mass and \mathbf{v}_{ab} is equal to the velocity difference $\mathbf{v}_a - \mathbf{v}_b$. The subscripts a and b are to identify the values of these quantities for particle a and particle b . The term Π_{ab} is the artificial viscosity required in SPH to correctly capture shocks, given by,

$$\Pi_{ab} = \begin{cases} -\alpha_{\text{SPH}} \frac{\bar{c}_{s,ab} \mu_{ab}}{\bar{\rho}_{ab}} + \beta_{\text{SPH}} \frac{\mu_{ab}^2}{\bar{\rho}_{ab}} & \text{if } \mu_{ab} < 0 \\ 0 & \text{otherwise} \end{cases} \quad (10)$$

where α_{SPH} and β_{SPH} are the SPH viscosity coefficients often taking typical values of 1 and 2 respectively (Lodato & Price 2010). μ_{ab} is the velocity field divergence over a scale length h , i.e. $\mu_{ab} = h \nabla \cdot \mathbf{v}$.

SPH being a Lagrangian method means that mass is automatically conserved and the continuity equation is satisfied for particles of equal mass. Since SPH is a mesh-free method, it is particularly useful in astrophysical problems where there is no fixed

boundary. There being no grid eliminates the issue of artificial grid alignment seen in moving and adaptive mesh codes where the fluid motion aligns with the grid axes. This is due to a numerical torque and can cause disc tearing (Hopkins 2015; Byerly et al. 2014).

Recently, the SPH code PHANTOM (Price et al. 2018) has been used to probe the effect of primary star mass on the fragmentation of protoplanetary discs (Cadman et al. 2020). Disc instability has also been investigated using GANDALF (Hubber, Rosotti & Booth 2017), an alternative SPH code, in Mercer & Stamatellos (2020). Well documented issues of SPH, particularly its treatment of viscosity, warrant the investigation into the effectiveness of alternate hydrodynamic codes.

3.2 Meshless Hydrodynamics

A combination of SPH and grid based codes could potentially provide the advantages of both methods without the associated disadvantages. AREPO (Weinberger, Springel & Pakmor 2019) is a moving-mesh code where the volume is partitioned with an exact Voronoi tessellation where cells can refine and derefine as needed. This method potentially suffers from highly irregular cell shapes introducing errors and an accuracy reduction in complicated flows.

A meshless method has the potential to improve upon these existing problems. Meshless methods use moving cells¹ to represent the volume where each cell takes on the mean values of fluid quantities it represents. Both MFM and MFV are meshless, Lagrangian methods which allow a continually adaptive resolution whilst conserving mass, momentum and energy. Meshless methods discretize the volume with a kernel but unlike in SPH, this kernel does not play a role in the hydrodynamics equations. Rather, the equations of fluid motion are derived from an exact representation of the volume partition (Hopkins 2015). The cells in MFM and MFV overlap and the fraction of the volume represented by cell a is given by

$$\psi_a(\mathbf{r}) = \frac{1}{\omega(\mathbf{r})} W(\mathbf{r} - \mathbf{r}_a, h), \quad (11)$$

$$\omega(\mathbf{r}) = \sum_b W(\mathbf{r} - \mathbf{r}_b, h), \quad (12)$$

where $\omega(\mathbf{r})^{-1}$ is a normalisation to ensure the whole volume is summed correctly such that the sum of the weights ψ is equal to 1 at every point in the volume. This

¹We refer to the volume domains associated with each particle in the meshless methods as ‘cells’. This should not be confused with the notion of cells in moving-mesh methods. Further to this, the ‘particles’ in meshless methods can be considered volume domain generating points but are referred to as particles throughout for brevity.

fractional representation of the volume means there is an overlap between cells across which a Riemann solver is used to calculate fluxes. The kernel W is used to associate a fraction of the volume to particle a . For 100% of the volume to be associated with the nearest particle, the function W has to be sharply peaked. This would recover an exact Voronoi tessellation and reproduce the behaviour of AREPO (Weinberger, Springel & Pakmor 2019).

MFV allows for a mass flux between cells, meaning that the mass in each cell is not constant. In discs this causes mass transfer outwards due to angular momentum advection. A special case of the finite volume method is MFM, which is characterised by its conservation of mass in each cell. This makes it particularly useful in applications featuring star and galaxy formation where self-gravity is important. The construction of the cells in MFM and MFV is identical, what differentiates them is the reference frame in which fluxes are calculated. In MFV the effective velocity of the frame $\mathbf{v}_{\text{eff}}^{\text{frame}}$ is zero and the Riemann problem is solved across the two cells. In MFM it is assumed that the volume distorts with the mean motion so that mass in two neighbouring cells is conserved. In this case, the frame has a velocity equal to that of the Riemann contact wave, given by $\mathbf{v}_{\text{eff}}^{\text{frame}} = S_*$

4 Viscosity treatments in hydrodynamic simulations

One of the key misgivings of SPH is its treatment of viscosity. Traditional SPH codes can produce numerical viscosity at an order of magnitude higher than other methods. This may lead to excessive angular momentum transfer which is of particular consequence in accretion discs. It follows from the SPH equations of motion that entropy is conserved. However, in realistic fluids, collisions between flows generate heat, and entropy increases in these shock regions. Therefore, for these shocks to be correctly captured, an artificial viscosity is required to dissipate velocity differences and convert kinetic energy to heat thus increasing entropy and reproducing the shock (Cullen & Dehnen 2010).

4.1 Standard artificial viscosity in SPH

An artificial pressure term Π_{ab} , is added to the SPH momentum and energy equations to correctly capture shocks. Π_{ab} is given by Lodato & Cossins (2011) as

$$\Pi_{ab} = \begin{cases} -\alpha_{\text{SPH}} \frac{\bar{c}_{s,ab} \mu_{ab}}{\bar{\rho}_{ab}} + \beta_{\text{SPH}} \frac{\mu_{ab}^2}{\bar{\rho}_{ab}} & \text{if } \mu_{ab} < 0 \\ 0 & \text{otherwise,} \end{cases} \quad (13)$$

where $\bar{\rho}_{ab}$ is the average density and $\bar{c}_{s,ab}$ is the average sound speed of particles a and b . The coefficients α_{SPH} and β_{SPH} are often set to 1 and 2 respectively. μ_{ab} is given by

$$\mu_{ab} = \frac{\bar{h}_{ab} \mathbf{v}_{ab} \cdot \mathbf{r}_{ab}}{|\mathbf{r}_{ab}|^2 + \epsilon \bar{h}_{ab}^2}, \quad (14)$$

where h is a characteristic smoothing length and the shorthand $A_{ab} = A_a - A_b$ is used in the case of the velocity \mathbf{v} and the position \mathbf{r} . The over-bar is used to indicate that the quantity takes on the mean value for particles a and b . The factor ϵ where $\epsilon \ll 1$ is used to avoid a singularity in the limit where $\mathbf{r}_{ab} \rightarrow 0$.

From this we can see that for receding pairs, $\Pi_{ab} = 0$ and so artificial viscosity only effects compressive flows, not those that expand (Cullen & Dehnen 2010). This is the standard method used for the treatment of viscosity in many SPH codes including GADGET (Springel 2005). In practice, this artificial viscosity produces nonphysical dissipation away from the shock regions causing, in the case of a protoplanetary disc, unrealistic angular momentum transport.

4.2 Morris and Monaghan formulation

This model of artificial viscosity is modified in the method of Morris & Monaghan (1997) which allows for a continually adaptive value of $\alpha_{\text{SPH},a}$ for each particle. This leads to the modification of α_{SPH} in Eq. (13) to instead take the average value of α for two particles a and b such that $\bar{\alpha}_{\text{SPH},ab} = (\alpha_{\text{SPH},a} + \alpha_{\text{SPH},b})/2$. This method has a lower limit of $\alpha = 0.1$ for all particles. Although the Morris & Monaghan (1997) method constitutes a significant improvement over the standard treatment of viscosity in SPH, any value of $\alpha > 0$ causes nonphysical angular momentum transport and dissipation.

4.3 The Balsara switch

One ‘switch’ to alleviate nonphysical angular momentum transport as a result of artificial viscosity in SPH was developed by Balsara (1995). The Balsara switch acts to reduce the artificial viscosity away from shocks by a factor \bar{f}_{ab} given by $\bar{f}_{ab} = (\bar{f}_a + \bar{f}_b)/2$ where

$$f_a = \frac{|\nabla \cdot \mathbf{v}_a|}{|\nabla \cdot \mathbf{v}_a| + |\nabla \times \mathbf{v}_a|}. \quad (15)$$

\mathbf{v}_a is the velocity of particle a (Balsara 1995). This factor multiplies the artificial pressure Π_{ab} , in the energy and momentum equations such that

$$\frac{du_a}{dt} = \frac{1}{2} \sum_b m_b \left(\frac{P_b}{\rho_b^2} + \frac{P_a}{\rho_a^2} + \bar{f}_{ab} \Pi_{ab} \right) \mathbf{v}_{ab} \cdot \nabla_a W_{ab}, \quad (16)$$

$$\frac{dv_a}{dt} = - \sum_b m_b \left(\frac{P_b}{\rho_b^2} + \frac{P_a}{\rho_a^2} + \bar{f}_{ab} \Pi_{ab} \right) \nabla_a W_{ab}. \quad (17)$$

where P is pressure, ρ is density, m is mass and \mathbf{v}_{ab} is equal to the velocity difference $\mathbf{v}_a - \mathbf{v}_b$. W_{ab} is the SPH kernel function where $W_{ab} = W(\mathbf{r}_a - \mathbf{r}_b, h)$.

In a Keplerian disc, the following are true:

$$|\nabla \times \mathbf{v}_a| = \left(\frac{GM}{4r^3} \right)^{1/2}, \quad (18)$$

$$|\nabla \cdot \mathbf{v}_a| = 0 \quad (19)$$

Convergent flow in the disc causes an increase in $|\nabla \cdot \mathbf{v}_a|$ and a subsequent increase in \bar{f}_a up to the limit of unity when $|\nabla \cdot \mathbf{v}_a| \gg |\nabla \times \mathbf{v}_a|$. This means that when the vorticity $|\nabla \times \mathbf{v}_a|$ dominates over the convergence i.e. in areas of stable Keplerian rotation, the artificial viscosity is in effect ‘switched off’. The results from Cartwright & Stamatellos (2010) indicate that this method of controlling artificial viscosity in

accretion discs suffers from nonphysically large values of f_a . The same work finds that, when using $|\nabla \cdot \mathbf{v}_a|$ as an indicator of convergence, particles form alignments in the leading direction. This causes a spurious increase in the value of f_a and reduces the effectiveness of the Balsara switch in ‘turning off’ artificial viscosity away from shocks.

4.4 The Cullen and Dehnen 2010 (CD10) switch

The Cullen & Dehnen (2010) switch (CD10 switch) for controlling artificial viscosity uses the total time derivative of the velocity divergence where a negative value of $\dot{\nabla} \cdot \mathbf{v}$ indicates a region where the convergence of the flow is steepened which is indicative of a pre-shock region while a positive value implies a post-shock region. The CD10 switch uses a limiter with the same functional form of Eq. (15) but with particular attention paid to limiting false detections of convergent flows. The limiter for the CD10 switch takes the form

$$\xi_a = \frac{|2(1 - R_a)^4 \nabla \cdot \mathbf{v}_a|^2}{|2(1 - R_a)^4 \nabla \cdot \mathbf{v}_a|^2 + |\nabla \times \mathbf{v}_a|^2}, \quad (20)$$

$$R_a = \frac{1}{\hat{\rho}_a} \sum_b \text{sign}(\nabla \cdot \mathbf{v}_b) m_b W_{ab}. \quad (21)$$

Here, $\hat{\rho}_a$ is the local estimate of the density at the position of particle a given by the kernel estimator. R_a indicates the presence of shocks using a sign function that takes a value of -1 when $\nabla \cdot \mathbf{v}_b < 0$

$$\text{sign}(\nabla \cdot \mathbf{v}_b) = \begin{cases} -1 & \text{if } \nabla \cdot \mathbf{v}_b < 0 \\ 0 & \text{if } \nabla \cdot \mathbf{v}_b = 0 \\ 1 & \text{if } \nabla \cdot \mathbf{v}_b > 0. \end{cases} \quad (22)$$

This means that in the presence of a shock, $R_a \approx -1$. This detection of shocks and improved limiter gives a much improved prescription of artificial viscosity in SPH which avoids false detections of shocks in complicated flows.

Cullen & Dehnen (2010) apply this method of controlling artificial viscosity in the context of a 2D Keplerian disc. The results for traditional SPH, the Morris & Monaghan (1997) method and the Balsara switch all show the disc breaks apart due to the viscous instability within a few inner orbital periods with only the CD10 method maintaining equilibrium after 5 periods.

4.5 Viscosity treatment with the Reimann approach

An alternative approach to shock capture in SPH is to solve the Reimann problem (RP) between particles. This reformulation of the SPH method was pioneered by Inutsuka (2002) and eliminates the need for the addition of an artificial viscosity to correctly capture shocks. A schematic of the RP in 1 dimension is shown in Fig. 3.

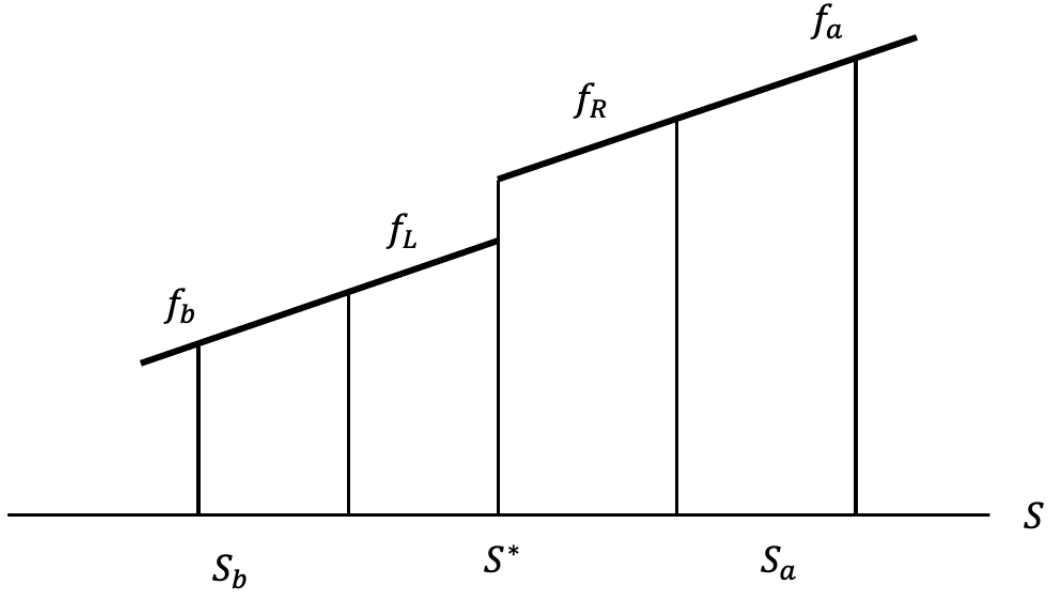


Figure 3: Schematic illustration of the Reimann Probelem in the vicinity of particles a and b where the function $f(S)$ is defined. The Reimann solver is used to calculate the value of the function at the interface S^* , adapted from Inutsuka (2002).

The RP is solved across the boundary between the two particles a and b to give the value of the function as the border, labelled S^* in Fig. 3. This Godunov-type SPH (GSPH) uses modified versions of the energy and momentum equations where the pressure terms for particles a and b is replaced by the solution of the RP such that Eqs. (8) and (9) become

$$\frac{dv_a}{dt} = - \sum_b m_b P^* \left(\frac{1}{\rho_b^2} + \frac{1}{\rho_a^2} \right) \nabla_a W_{ab}, \quad (23)$$

$$\frac{du_a}{dt} = \frac{1}{2} \sum_b m_b P^* \left(\frac{1}{\rho_b^2} + \frac{1}{\rho_a^2} \right) \mathbf{v}_{ab} \cdot \nabla_a W_{ab}, \quad (24)$$

where P^* is the value of the linearly interpolated value of pressure, found at the boundary between the two particles by solving the RP (Cha & Whitworth 2003).

5 Protostellar Disc Initial Conditions

The disc in each simulation is constructed based on a set of initial conditions that define the density, temperature and velocity at every point in the system. The temperature and density profile exponents, disc mass and radius as well as the star mass are free parameters.

5.1 Surface and Volume Density

In their investigation into the initial stages of evolution in protoplanetary discs, Lin & Pringle (1990) find evidence to suggest that the surface density distribution is of the form $\Sigma \propto R^{-p}$ where R is the mid-plane orbital radius. In this work we use the distribution

$$\Sigma = \Sigma_0 \left(\frac{R_0^2}{R_0^2 + R^2} \right)^{\frac{p}{2}}, \quad (25)$$

where Σ_0 is the surface density at a mid-plane radius $R=0$, R_0 is the softening radius, used to prevent the density becoming nonphysically large close to the star, and p is the density profile exponent.

The surface density Σ , at radius R on the mid-plane is given by the integral of the volume density ρ , through the vertical direction z on the disc

$$\Sigma(R) = \int_{-z_0(R)}^{z_0(R)} \rho(R, z) dz, \quad (26)$$

where $z_0(R)$ is the disc thickness at R . We assume a sinusoidal volume density profile describing the density drop with distance from the mid-plane

$$\rho(R, z) = \rho(R, 0) \cos \left[\frac{\pi z}{2z_0(R)} \right], |z| < z_0(R). \quad (27)$$

Integrating along z , solving for $\rho(R, 0)$ and substituting the surface density using Eq. (25) gives

$$\rho(R, 0) = \frac{\pi \Sigma_0}{4z_0(R)} \left(\frac{R_0^2}{R_0^2 + R^2} \right)^{\frac{p}{2}}. \quad (28)$$

Thus, we finally have for the volume density

$$\rho(R, z) = \frac{\pi \Sigma_0}{4z_0(R)} \left(\frac{R_0^2}{R_0^2 + R^2} \right)^{\frac{p}{2}} \cos \left[\frac{\pi z}{2z_0(R)} \right]. \quad (29)$$

Plots of the volume density profile and face-on projection of the disc are shown in the left and right panels of Fig. 4, respectively.

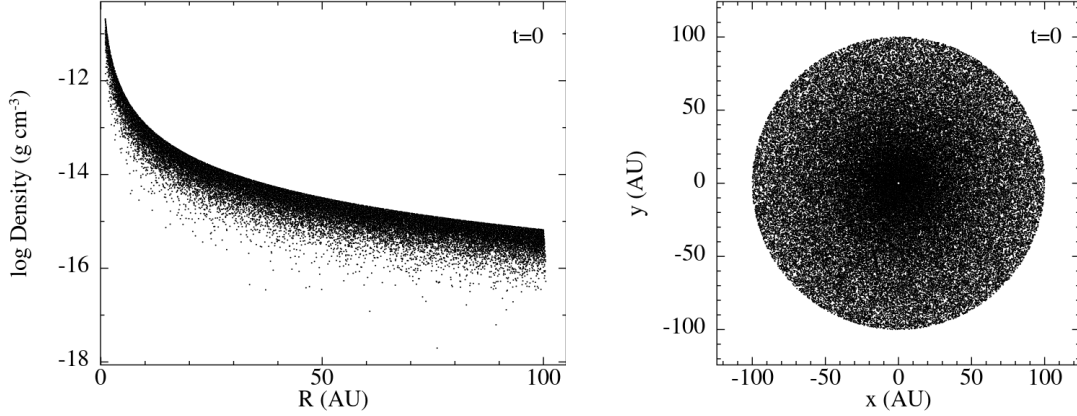


Figure 4: Initial density profile and face-on projection for a $0.1 M_{\odot}$ disc extending to 100 AU with a temperature profile exponent $q = 0.5$, a density profile exponent $p = 1$. We represent the disc using 1×10^5 particles which are distributed in space to reproduce the density profile given in Eq. (29)

To adequately model planet formation in fragmenting discs, we require the simulated disc to evolve beyond a point after which the specific initial setup is not important. Once the disc starts evolving it will eventually settle to its equilibrium state. We refer to the period before this point as the time taken for the disc to relax. Due to the short timescale on which planets form in fragmenting discs, we aim to minimise this relaxation time to accurately capture the evolution of the disc at early times.

A better estimate of the vertical disc density profile than the sinusoidal approach of Eq. (29) is to take into account the hydrostatic equilibrium in the direction vertical to the disc mid-plane (z -direction).

The vertical component of the gravitational acceleration, g_z must balance the vertical pressure gradient, i.e.

$$\frac{1}{\rho} \frac{dP}{dz} = -g_z, \quad (30)$$

We assume that the disc is in Keplerian rotation and

$$g_z = \Omega^2 z, \quad (31)$$

where P is the pressure, ρ is the density, z is the height above the mid-plane and Ω is the Keplerian angular velocity $\Omega = \left(\frac{GM_*}{R^3}\right)^{1/2}$, where G is the gravitational constant and M_* is the stellar mass. By writing the pressure as $P = \rho c_s^2$ where c_s is the sound speed, we can solve for ρ by assuming that the disc is geometrically thin such that

$z \ll R$. This gives the vertical density profile

$$\rho(R, z) = \rho(R, 0) \exp\left(-\frac{z^2}{2H^2}\right), \quad (32)$$

where H is the disc scale height and $\rho(R, 0)$ is equal to

$$\rho(R, 0) = \frac{\Sigma}{\sqrt{2\pi}} \frac{1}{H}, \quad (33)$$

where Σ is the surface density at R . Following tests that compare the initial conditions to the disc at $t = 5000$ yrs, we find that the profile in Eq. (32) produces a disc with a shorter relaxation time and as a result we choose to adopt this for following simulations.

5.2 Disc Temperature

A protoplanetary disc is heated by stellar irradiation and viscous processes. In the case of a geometrically thin passive disc, one with no viscous dissipation, the radiation flux incident on a unit area is proportional to $\frac{1}{R^3}$ (Hartmann et al. 1998). Therefore the incident flux and the emitted flux, assuming the disc behaves like a blackbody are given by

$$F_{\text{incident}} \propto \sigma T_*^4 \left(\frac{R}{R_*}\right)^{-3}, \quad (34) \quad F_{\text{emitted}} \propto \sigma T_d^4. \quad (35)$$

Eq. (34) and Eq. (35) can be equated to give the passive disc temperature profile

$$T_d(R) \propto T_* \left(\frac{R}{R_*}\right)^{-\frac{3}{4}}. \quad (36)$$

For the case of an active disc where heating is provided by viscous dissipation we assume that half of the energy released by the inward spiral of matter is radiated away as blackbody radiation such that

$$\frac{GM_* \dot{M}}{2R} \frac{\Delta R}{R} \approx 2 \times 2\pi R \Delta R \sigma T_d^4(R), \quad (37)$$

and so

$$T_d(R) = \left(\frac{GM_* \dot{M}}{8\pi\sigma R^3}\right)^{-\frac{1}{4}}. \quad (38)$$

From Eq. (36) and Eq. (38), we can see that both disc temperature profiles vary according to $T_d(R) \propto R^{-q}$, where $q = \frac{3}{4}$.

The presence of discs around young stars is often indicated by an infrared excess in the spectral energy distribution (SED) as a result of the absorption and re-emission of stellar radiation at longer wavelengths. The slope of the SED is connected to the temperature profile exponent and SED observations of pre-main sequence stars suggest values of q between 0.3 and 0.8 (Andrews et al. 2011).

In this study we choose a locally isothermal temperature profile such that the temperature of the disc at each radius R is

$$T_d(R) = \left[T_0^2 \left(\frac{R^2 + R_0^2}{\text{AU}^2} \right)^{-q} + T_\infty^2 \right]^{\frac{1}{2}}, \quad (39)$$

where T_0 is the temperature at 1 AU, T_∞ is the temperature far away from the star, R_0 is the softening radius that prevents infinitely large temperatures close to the star. The temperature profile for a typical disc is plotted in the left panel of Fig. 5.

5.3 Disc Rotation

We set the disc into Keplerian rotation such that the velocity v at radius R on the mid-plane is

$$v(R) = \left(\frac{GM_*}{R} \right)^{1/2}, \quad (40)$$

where M_* is the mass of the central star and G is the gravitational constant. Since this disc is self-gravitating, its mass is important, leading to the necessary modification of the above equation,

$$v(R) = \left(\frac{G[M_* + M_{\text{disc}}(< R)]}{R} \right)^{1/2}, \quad (41)$$

where $M_{\text{disc}}(< R)$ is the mass of the disc interior to radius R . A plot of the velocity profile for a typical disc is shown in the right panel of Fig 5 .

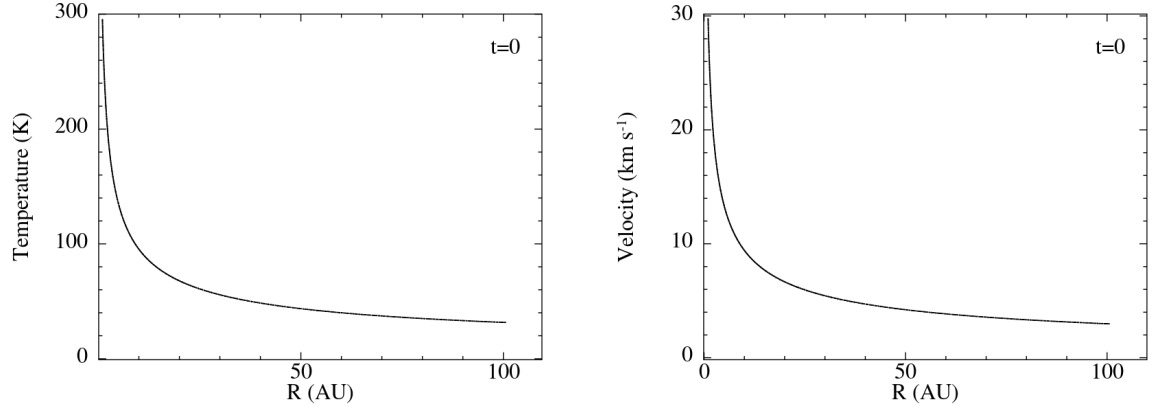


Figure 5: The same disc setup as in Fig 4. The temperature profile (*left*) and velocity profile (*right*) are constructed using Eq. (39) and Eq. (41), respectively.

6 Evaluating the effective disc viscosity in SPH simulations

Controlling the disc viscosity by varying the value of α_{SPH} is common practise in modelling viscous accretion discs. Several previous authors (e.g. Price et al. 2018; Lodato & Pringle 2007) have concluded that the shear component of viscosity can be written in terms of artificial viscosity

$$\nu_{\text{AV}} \approx \frac{1}{10} \alpha_{\text{SPH}} c_s h, \quad (42)$$

where c_s is the sound speed and h is the smoothing length. The α parameterization of viscosity (Shakura & Sunyaev 1973) represents the kinematic viscosity ν , with an ‘effective - alpha’ α_{SS} ,

$$\nu = \alpha_{\text{SS}} c_s H. \quad (43)$$

Eqs. (42) and (43) imply that the effective viscosity for a disc with artificial viscosity parameter α_{SPH} is given by

$$\alpha_{\text{SS}} = \frac{1}{10} \alpha_{\text{SPH}} \frac{\langle h \rangle}{H}, \quad (44)$$

where $\langle h \rangle$ is the average value of the smoothing length at a given radius and H is the disc scale height (Price et al. 2018).

We calculate the effective viscosity using an analytical model of disc evolution and compare the resulting values to the radially averaged values calculated by Eq. (44). The surface density evolution of a geometrically thin disc subject to viscous angular momentum transport is given by

$$\frac{\partial \Sigma}{\partial t} = \frac{3}{R} \frac{\partial}{\partial R} \left[R^{1/2} \frac{\partial}{\partial R} (\nu \Sigma R^{1/2}) \right], \quad (45)$$

where Σ is the surface density, R is the mid-plane radius and ν is the kinematic viscosity (Pringle 1981). With the assumption that the viscosity in the disc is represented by a power law of the form $\nu \propto R^\gamma$ and is independent of time. With this assumption in place, Eq. (45) has the similarity solution (Lynden-Bell & Pringle 1974)

$$\Sigma(R, t) = \frac{M_{\text{D}}(0)(2 - \gamma)}{2\pi R_0^2 r^\gamma} \tau^{(5/2 - \gamma)/(2 - \gamma)} \exp \left[-\frac{r^{2 - \gamma}}{\tau} \right], \quad (46)$$

where we have made the substitutions $r = \frac{R}{R_0}$, R_0 being the radius interior to which 60% of the mass is contained and $\tau = \frac{t}{t_\nu} + 1$ where t_ν is the viscous scaling time given by

$$t_\nu = \frac{R_0^2}{[3(2 - \gamma)^2 \nu(R_0)]}. \quad (47)$$

The mass accretion rate on to the central star is then given by

$$\dot{M}_* = \frac{M_D(0)}{2(2-\gamma)t_\nu} \tau^{-(5/2-\gamma)/(2-\gamma)} \quad (48)$$

We assume that the disc is locally vertically isothermal and in Keplerian rotation such that $H = c_s/\Omega$ and $\Omega = (GM_*/R^3)^{1/2}$ and therefore Eq. (43) can be expressed as

$$\nu = \alpha_{\text{SS}} \frac{c_s^2}{\Omega}. \quad (49)$$

If the temperature is represented by the power law $T \propto R^{-q}$ then

$$\nu \propto R^{\frac{3}{2}-q} \propto R^\gamma, \quad (50)$$

it is assumed in the model that $q = 0.5$ and therefore $\gamma = 1$ (Hartmann et al. 1998).

With this prescription of viscosity we can rewrite Eq. (48), making the substitution from Eq. (47)

$$\dot{M}_* = \frac{3}{2} \frac{M_D(2-\gamma)\alpha_{\text{SS}}c_s^2}{R_0^2\Omega} \left(\frac{3(2-\gamma)^2\alpha_{\text{SS}}c_s^2t}{R_0^2\Omega} + 1 \right)^{-(5/2-\gamma)/(2-\gamma)}. \quad (51)$$

Eq. (51) represents the theoretical time evolution of mass accretion rate. We perform simulations of high and low mass discs and calculate the accretion rate on to the central star. We then use Eq. (51) with the effective viscosity α_{SS} and viscosity exponent γ as free parameters in a fit that is applied to the calculated mass accretion rate. These analytical values of α_{SS} are compared with those calculated using the SPH formalism in Eq. (44).

We use the SPH code PHANTOM (Price et al. 2018) to model $0.01 M_{\odot}$ and $0.2 M_{\odot}$ discs consisting of 200,000 particles around a $1 M_{\odot}$ star with an accretion radius of 1 AU. Each disc has an inner radius of $R_{\text{in}} = 1$ AU and an outer radius $R_{\text{out}} = 100$ AU. The evolution of the disc is followed for 5000 years which, for a disc of this extent, equates to 5 orbits of the outer radius. The discs are locally isothermal, i.e. the temperature depends only on the distance from the star on the disc mid-plane. The temperature profile exponent is set to $q = 0.5$ and $T_0 = 300$ K (see Eq. (39)). Tests using a surface density profile with the exponent $p = 1$ show that the surface density profile at $t = 5000$ years is steeper than in the initial conditions. To limit the time taken for the disc to evolve to an equilibrium state we adopt a steeper surface density profile with $p = 2.05$. Fig. 6 shows surface density plots of both disc masses at $t = 5000$ years.

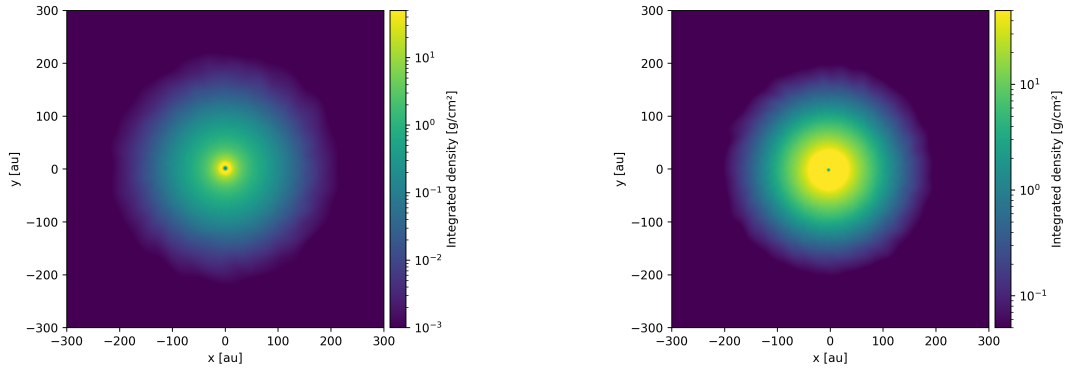


Figure 6: Surface density plots for a $0.01 M_{\odot}$ disc (*left*) and a $0.2 M_{\odot}$ (*right*) disc at $t = 5000$ years. We use PLONK (Mentiplay 2019) to produce these plots.

In each simulation we investigate a different value for artificial viscosity parameter α_{SPH} ; the three values chosen are 0.1, 0.5 and 1.0. We set $\beta_{\text{SPH}} = 2$ for all simulations. The stellar mass accretion rates \dot{M} from the simulations are plotted as a function of time in units of $M_{\odot} \text{ yr}^{-1}$ for the $0.01 M_{\odot}$ discs and $0.2 M_{\odot}$ discs in the left and right panels of Fig. 7, respectively.

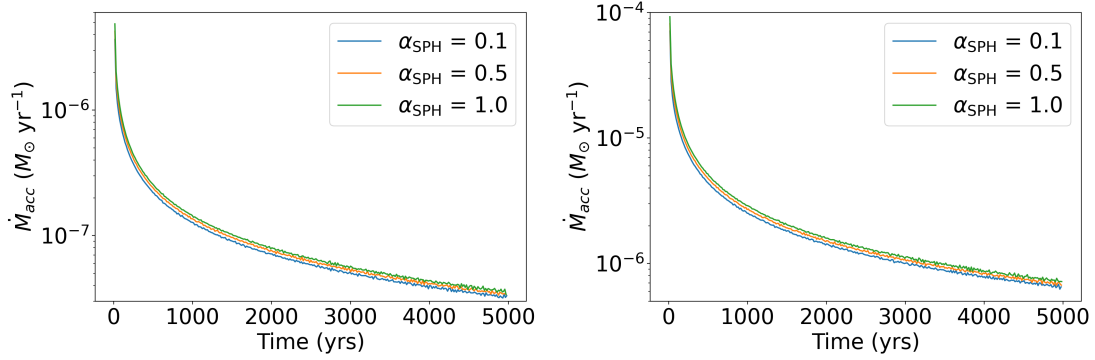


Figure 7: The mass accretion rates for the three $0.01 M_{\odot}$ discs (*left*) and three $0.2 M_{\odot}$ discs (*right*) with artificial viscosity values $\alpha_{\text{SPH}} = 0.1, 0.5$ and 1.0 . The more viscous disc facilitates a higher stellar accretion rate.

In both cases, a disc with a higher value of α_{SPH} more efficiently transports angular momentum radially outwards, facilitating stellar accretion at an increased rate. Fig. 7 illustrates this expected relationship between \dot{M} and α_{SPH} . We use Eq. (51) to fit the mass accretion rate calculated in the simulations with the Shakura and Sunyaev effective alpha α_{SS} and the radial exponent of viscosity γ as free parameters. The fits are performed from 2500 yrs - 5000 yrs to accommodate the settling period of the disc.

Table 1 shows the resulting values for the effective viscosity and viscosity exponent γ at the three artificial viscosities tested in the $0.01 M_{\odot}$ and $0.2 M_{\odot}$ discs, respectively.

	Disc mass = $0.01 M_{\odot}$		Disc mass = $0.2 M_{\odot}$	
α_{SPH}	α_{SS}	γ	α_{SS}	γ
0.1	$(1.6 \pm 0.03) \times 10^{-3}$	(-25 ± 0.12)	$(1.6 \pm 0.03) \times 10^{-3}$	(-25 ± 0.12)
0.5	$(1.9 \pm 0.05) \times 10^{-3}$	(-24 ± 0.13)	$(1.9 \pm 0.04) \times 10^{-3}$	(-23 ± 0.13)
1.0	$(2.2 \pm 0.07) \times 10^{-3}$	(-22 ± 0.12)	$(2.2 \pm 0.05) \times 10^{-3}$	(-22 ± 0.12)

Table 1: The resulting values of α_{SS} and γ from fitting the stellar mass accretion rate with the analytic model in Eq. (51) for both discs.

We also calculate the radially averaged effective disc viscosity by using Eq. (44), i.e. from SPH formalism. Fig. 8 shows the radially averaged values of α_{SS} for both disc masses at $t = 0$ yr and $t = 3500$ yrs in the left and right hand side panels respectively. We see that the SPH formalism results in viscosities of ≈ 0.01 , 0.03 , and 0.06 , whereas from the analytic model fitting finds viscosities around 0.002 , with very slight increase of the effective viscosity as α_{SPH} increases. This could be a result of the assumption made in the analytical model that $\nu = \alpha_{\text{SS}} \frac{c_s^2}{\Omega} \propto R^\gamma$ and is independent of time. It may also be attributed to a numerical viscosity which, for discs with $\alpha_{\text{SS}} < 0.01$ may play a role in angular momentum transport (Clarke 2009).

It is clear that α_{SS} for $t = 3500$ yrs drops as $\alpha_{\text{SS}} \propto R^{-x}$ inside 15 AU and is therefore inconsistent with the assumption made in the analytical model that α_{SS} is constant with radius.

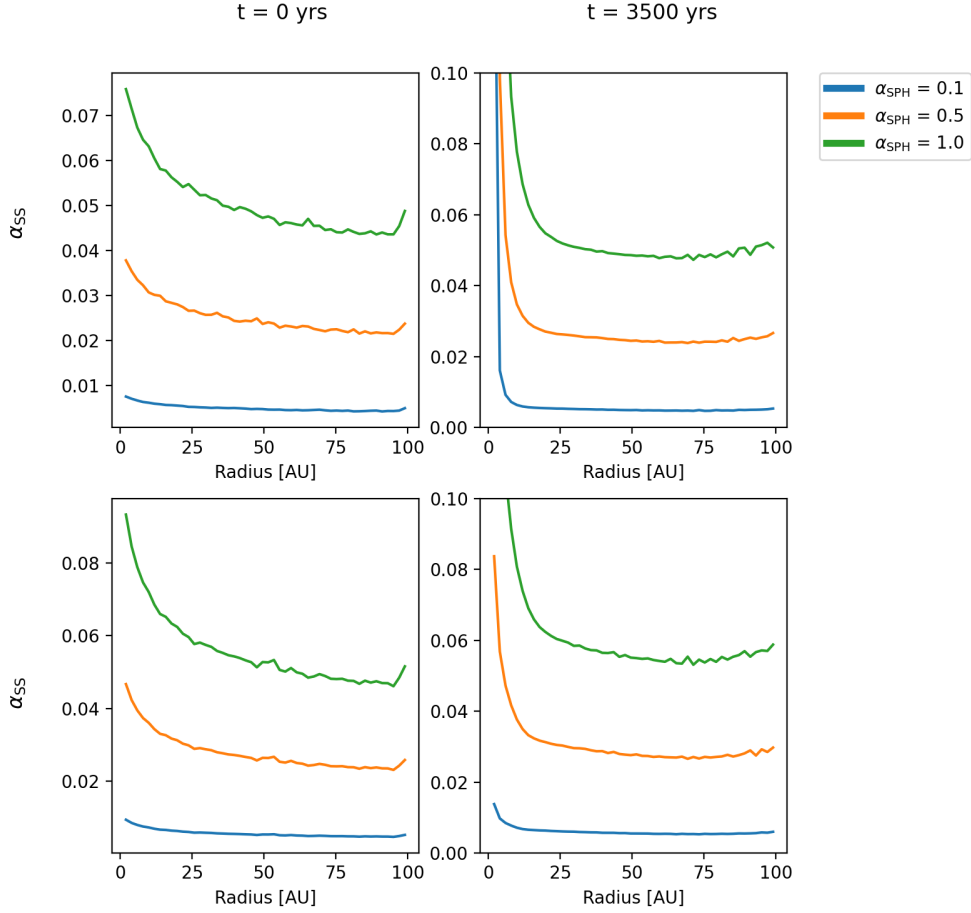


Figure 8: Radially averaged values of α_{SS} at $t = 0$ yrs (*left*) and $t = 3500$ yrs (*right*). The upper two panels show the radial profiles for the $0.01 M_\odot$ discs, the lower are those corresponding to the $0.2 M_\odot$ discs.

This means that inside a radius of ≈ 15 AU the radial dependence of kinematic viscosity is such that $\nu \propto R^{1-x}$, which justifies the negative values of γ in Table 1 and could explain the discrepancy we see between the radially averaged value of α_{SS} and those calculated from fitting \dot{M} . The radially averaged profiles of α_{SS} in Fig. 8 are mostly consistent with each other across both disc masses. The values of effective viscosity outside ≈ 15 AU are marginally higher in the $0.2 M_{\odot}$ disc but largely consistent with those found for the less massive disc.

For a more massive disc, we would expect the effective viscosity to be larger than for a low mass disc due to the effect of gravity aiding the redistribution of angular momentum. For a sufficiently massive disc that cools on a short enough timescale, the Toomre parameter in Eq. (1) falls below 1. This is the threshold for gravitational instability. In this regime, the disc can form spiral arms which facilitate the transfer of angular momentum radially outwards and would result in a higher measured value for effective viscosity. Fig. 9 shows the radial profiles of Toomre Q at 5000 yrs for both disc masses that we have simulated with the three values of α_{SPH} we investigate.

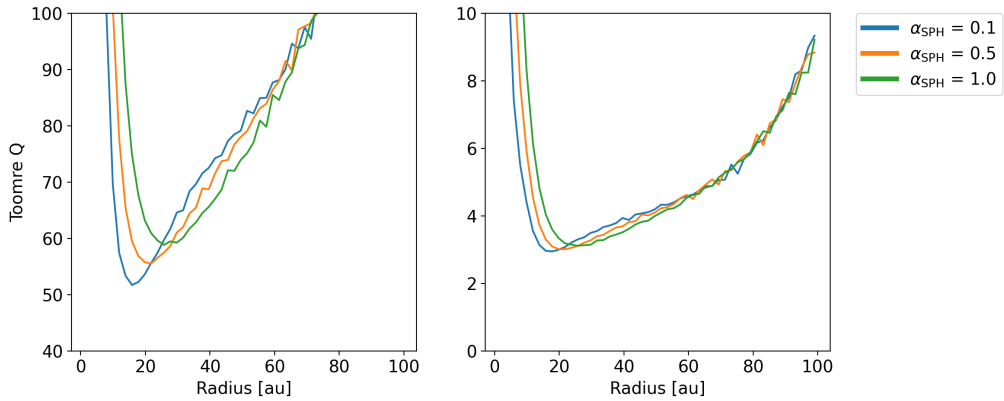


Figure 9: Radially averaged values of Toomre Q at $t = 5000$ yrs for the $0.01 M_{\odot}$ disc (*left*) $0.2 M_{\odot}$ disc (*right*). In both cases, the disc is stable with the value of Q being above 1.

The right panel of Fig. 9 shows that in the high mass disc, the value for Q is always above 1 and so the disc is always in the regime of gravitation stability and therefore does not develop any spiral arms to redistribute angular momentum. This illustrates why the measured values of α_{SS} for the high mass disc are not significantly larger than those in the low mass disc. We attribute this behaviour to the disc temperature being high. For a massive disc with a higher temperature profile exponent q and therefore a steeper temperature profile, we expect spiral structure to form and the values of α_{SS} to be significantly larger.

We conclude that the value of the effective viscosity in SPH simulation of discs is uncertain, as different methods provide results that differ by approximately an order of magnitude. The values calculated by the analytical model also do not show the expected variance between simulations with different values of artificial viscosity. This could be attributed to a numerical viscosity present in discs with low α_{SPH} which could result in a larger value of “background” effective viscosity.

7 Future work

Initially, further work will focus on implementing the radiative transfer method of Stamatellos et al. (2007) into PHANTOM and comparing disc simulations with alternative SPH code SEREN. Following this, we will investigate the formation of clumps in the disc that form as a result of disc instability and implement a method for tracking these clumps to follow their early evolution. We will develop a polytropic model to describe these clumps in favour of the existing sink particle method, this will allow for more detailed evaluation of clumps forming in discs. Following this, we will compare clump evolution to highly detailed 2D simulations that will include clump rotation and further expand the parameter space of fragment properties to investigate how they effect the properties of planets. These planet properties will be compared to observations of exoplanets.

8 Timeplan

	Year Two				Year 3			
	Q1 Mar - Jun	Q2 Jun - Sep	Q3 Sep - Dec	Q4 Dec - Mar	Q5 Mar - Jun	Q6 Jun - Sep	Q7 Sep - Dec	Q8 Dec - Mar
Implement radiative transfer								
Implement tracking of clumps/fragments								
Develop a polytropic model for fragments								
Run simulations with different disc properties								
Analyse the simulation results								
Compare the evolution with 2D simulations								
Complete annual progression								
Expand parameter space of initial fragments								
Calculate the properties of planets								
Compare with observed exoplanets								
Write thesis								

9 Thesis Structure

- i Abstract
- ii Contents
- iii Acknowledgements
- 1. Introduction
 - i Numerical hydrodynamics
 - ii Treatments of viscosity in hydrodynamic simulations
 - iii Disc fragmentation mechanism
- 2. Simulations
 - i Protostellar disc initial conditions
 - ii Clump tracking
 - iii Radiative transfer
 - iv Polytropic modelling of clumps
 - v results and discussion
- 3. Clump analysis
 - i Clump evolution in 2D models including rotation
 - ii 2D models of expanded fragment parameter space
- 4. Planet analysis
 - i Dependence of planet properties on fragment properties
 - ii Comparison with observed exoplanets
 - iii Discussion
- 5. Conclusions and future work
- 6. Bibliography
- 7. Appendices

References

- Andrews S. M., Wilner D. J., Espaillat C., Hughes A. M., Dullemond C. P., McClure M. K., Qi C., Brown J. M., 2011, *Astrophysical Journal*, 732
- Armitage P. J., 2010, *Astrophysics of Planet Formation*, 1st edn. Cambridge University Press
- Balsara D. S., 1995, *Journal of Computational Physics*, 121, 357
- Boss A. P., 2011, *Astrophysical Journal*, 731
- Byerly Z. D., Adelstein-Lelbach B., Tohline J. E., Marcello D. C., 2014, *The Astrophysical Journal Supplement Series*, 212, 23
- Cadman J., Rice K., Hall C., Haworth T. J., Biller B., 2020, *Monthly Notices of the Royal Astronomical Society*, 000
- Cartwright A., Stamatellos D., 2010, *Astronomy and Astrophysics*, 516, 1
- Cha S. H., Whitworth A. P., 2003, *Monthly Notices of the Royal Astronomical Society*, 340, 73
- Clarke C. J., 2009, *Monthly Notices of the Royal Astronomical Society*, 396, 1066
- Cullen L., Dehnen W., 2010, *Monthly Notices of the Royal Astronomical Society*, 408, 669–683
- Damjanov I., Jayawardhana R., Scholz A., Ahmic M., Nguyen D. C., Brandeker A., van Kerkwijk M. H., 2007, *The Astrophysical Journal*, 670, 1337–1346
- Dodson-Robinson S. E., Veras D., Ford E. B., Beichman C. A., 2009, *Astrophysical Journal*, 707, 79
- Gutermuth R. A. et al., 2008, *The Astrophysical Journal*, 674, 336
- Haisch, Jr. K. E., Lada E. A., Lada C. J., 2001, *The Astrophysical Journal*, 553, L153
- Hartmann L., Calvet N., Erik G., D’Alessio P., 1998, *Astrophysical Journal*, 495, 385
- Hernandez J. et al., 2007, *The Astrophysical Journal*, 662, 1067
- Hopkins P. F., 2015, *Monthly Notices of the Royal Astronomical Society*, 450, 53
- Hubber D. A., Rosotti G. P., Booth R. A., 2017, *Monthly Notices of the Royal Astronomical Society*, 473, 1603–1632

- , 2018, *Monthly Notices of the Royal Astronomical Society*, 473, 1603
- Inutsuka S. I., 2002, *Journal of Computational Physics*, 179, 238
- Lada C. J. et al., 2006, *The Astronomical Journal*, 131, 1574
- Lin D. N. C., Pringle J. E., 1990, *The Astrophysical Journal*, 358, 515
- Lodato G., Cossins P. J., 2011, *European Physical Journal Plus*, 126, 1
- Lodato G., Price D. J., 2010, *Monthly Notices of the Royal Astronomical Society*, 405, 1212
- Lodato G., Pringle J. E., 2007, *Monthly Notices of the Royal Astronomical Society*, 381, 1287
- Lynden-Bell D., Pringle J. E., 1974, *Monthly Notices of the Royal Astronomical Society*, 168, 603
- Mentiply D., 2019, *Journal of Open Source Software*, 4, 1884
- Mercer A., Stamatellos D., 2020, *Astronomy & Astrophysics*, 116, 1
- Morris J. P., Monaghan J. J., 1997, *Journal of Computational Physics*, 136, 41
- NASA, 2021, NASA Exoplanet Archive. <https://exoplanetarchive.ipac.caltech.edu/>, [Online; accessed 30/3/21]
- Price D. J. et al., 2018, *Publications of the Astronomical Society of Australia*, 35
- Pringle J. E., 1981, *Annual Review of Astronomy and Astrophysics*, 19, 137
- Shakura N. I., Sunyaev R. A., 1973, , 500, 33
- Sicilia-Aguilar A. et al., 2006, *The Astrophysical Journal*, 638, 897
- Springel V., 2005, *Monthly Notices of the Royal Astronomical Society*, 364, 1105
- Stamatellos D., Whitworth A. P., 2009, *Monthly Notices of the Royal Astronomical Society*, 400, 1563
- Stamatellos D., Whitworth A. P., Bisbas T., Goodwin S., 2007, *Astronomy and Astrophysics*, 475, 37
- Stone J. M., Gardiner T. A., Teuben P., Hawley J. F., Simon J. B., 2008, , 178, 137
- Weinberger R., Springel V., Pakmor R., 2019